

Strong frequency-dependent beam steering dynamics, Zitterbewegung effect, and Klein tunneling in a ternary plasmonic-dielectric superlattice

Zhenzhen Liu ¹, Guochao Wei,¹ Dasen Zhang,¹ Wenqing Chen,¹ Lei Sun ², Jia Li,³ and Jun Jun Xiao ^{1,*}

¹*Shenzhen Engineering Laboratory of Aerospace Detection and Imaging, College of Electronic and Information Engineering, Harbin Institute of Technology (Shenzhen), Shenzhen 518055, China*

²*Institute of Microscale Optoelectronics (IMO), Shenzhen University, Shenzhen 518060, China*

³*Materials Interfaces Center, Shenzhen Institute of Advanced Technology, Chinese Academy of Sciences, Shenzhen 518055, China*



(Received 2 February 2021; revised 15 April 2021; accepted 28 April 2021; published 12 May 2021)

Band structures are intrinsically influenced by the mode interaction in waveguide array, which can support many intriguing phenomena such as negative refraction, on-chip lensing, and quantum-analog dynamics like Bloch oscillation and topological interface transportation. Multiple branches of band may emerge due to the comprehensive mode interactions associated with high-order photonic modes supported in high refractive index dielectric waveguide. Furthermore, the number of photonic modes confined in a high-index waveguide is determined by both the width and working frequency. Hence, the mode interaction and resultant band structure can be effectively tuned by the frequency. As such, a diversity of equipfrequency contours could be generated and modulated among a wide frequency range, which, however, remains largely unexplored. Here, we present several frequency-determined beam dynamics in a composite ternary plasmonic-dielectric waveguide array, including collimation effect, angle-dependent beam branching/multibranching, conicallike beam diffraction. Based on the evolution of the band structure, photonic Zitterbewegung effect and Klein tunneling can also be observed. In contrast to the coherent coupling between symmetric and antisymmetric modes that gives rise to the photonic Zitterbewegung effect, we show that three-mode coherent coupling in the ternary system can yield a superimposed extreme oscillation of the beam. This represents an extension of the general Zitterbewegung effect in photonic system. Additionally, the Klein tunneling sandwiched in two types of artificial waveguide arrays with different Dirac points is demonstrated, and approximately unimpeded penetration is exhibited. The configurations discussed here can be readily implemented in on-chip systems for a variety of potential applications including wave routing, selectively directional coupling, and multiplexing.

DOI: [10.1103/PhysRevB.103.195415](https://doi.org/10.1103/PhysRevB.103.195415)

I. INTRODUCTION

Optical waveguide array is an important system for photonic integration and an ideal platform for optical simulation research [1–5]. Due to the discretized nature of the waveguide array, this system can mimic the regular atom arrangement in crystalline lattices. As such, they can simulate many quasi-particle behavior in condensed matter physics, such as the Zitterbewegung effect and the topological localization [2,6–9]. On the other hand, waveguide arrays can be applied to flexibly control light on chip, including both the dispersion and propagation. Through the engineering of the interwaveguide coupling characteristics, a lot of interesting wave dynamics have been demonstrated, such as negative refraction [10–12], deep-subwavelength focusing [13,14], and Bloch oscillation [15].

Notably, planar waveguide arrays have been actively investigated in both the fundamental and experimental aspects [16–20]. With an effective negative index [21–23], the waveguide arrays can mimic the hyperbolic metamaterials, wherein many of the metamaterials with unusual properties and func-

tionalties can be realized, particularly the superdiffraction limit imaging [10]. Additionally, a well-engineered negative dispersion can be achieved by a curved all-dielectric waveguide array [24]. Generally, the dispersion engineering can be assisted by the mode-coupling model. Basically, a 2×2 effective Hamiltonian is used to describe the two-mode coupling case. For example, surface-plasmon localized modes at both sides of the metal layer are coupled together which lead to negative dispersion. While for composite plasmonic-dielectric waveguide arrays, photonic modes coupled together, respectively, via metal and dielectric layers can be understood as a generalized Su-Schrieffer-Heeger model [25]. Then Dirac points (DPs) at the Brillouin zone (BZ) center [16–20] and the conicallike beam diffractions were observed [25]. Additionally, by suitably tuning the coupling in the waveguide arrays, transitions between different topological phases can happen, and corresponding edge states may emerge [7,20]. It is noteworthy that the mode coupling plays an important role in constructing the required dispersion and controlling the propagation of light [26]. By virtue of degrees of geometry and frequency, the conicallike diffraction, the induced photonic Zitterbewegung effect [27,28], and Klein tunneling [26,29] have been widely investigated [30]. However, multiple mode coupling and resultant behaviors have not been carefully

*Corresponding author: eixiao@hit.edu.cn

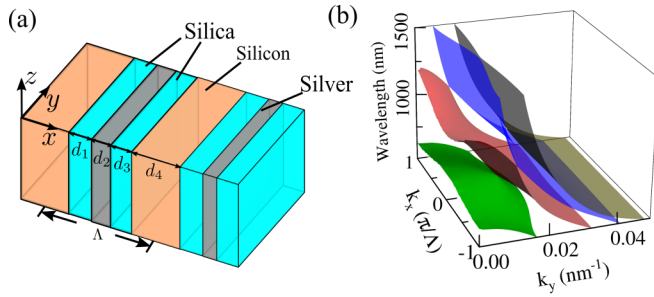


FIG. 1. (a) Schematic of the planar waveguide array with unit cell period $\Lambda = \sum_{i=1}^4 d_i$. (b) The dispersion in the space (k_x, k_y, λ) . The geometries are $d_1 = 50$ nm, $d_2 = 10$ nm, $d_3 = 50$ nm, $d_4 = 200$ nm.

reported, particularly for both plasmonic and photonic modes. Due to the existence of multiple high-order photonic modes, the intrinsic interactions become quite complex, which may give rise to a diversity of band dispersions and a variety of light propagation patterns. Thus, it would be desirable to investigate the beam dynamics which would greatly extend the functionalities of light transportation in such waveguide arrays.

In this paper, we investigate the beam dynamics in planar plasmonic-dielectric waveguide arrays (consisting of three components and four layers) among a wide frequency region. Firstly, for relatively short wavelengths, the waveguide arrays can support the higher-order photonic modes in the high-index dielectric waveguide. As such, three or four branches of mode dispersion are present, giving rise to the beam multibranching. More importantly, we show that, for two adjacent dispersion branches around the DP, the back-and-forth coherent coupling between the symmetric and antisymmetric modes raises the oscillation of the beam, which mimics the Zitterbewegung effect. More interestingly, the beam oscillation could be faster when an additional mode (granted by the carefully designed ternary system) is involved in the coupling process. Additionally, the Klein tunneling can be observed in a heterojunction by sandwiching two types of waveguide arrays with shifted DPs. Note that without loss of generality, we consider a multilayered plasmonic-dielectric superlattice structure to model the beam dynamics, while we believe that for strongly coupled waveguide arrays in a quasi-three-dimensional (3D) planar configuration, similar results are expected.

II. FREQUENCY-DEPENDENT BEAM STEERING DYNAMICS

Figure 1(a) shows the schematic of the considered waveguide arrays. It consists of a silver layer sandwiched by two silica layers. The sandwich structure is connected by a silicon slab periodically. The layers are of thickness d_1 , d_2 , d_3 , and d_4 , as shown in Fig. 1(a). The refractive indices of silica and silicon are $n_1 = n_3 = 1.44$ and $n_4 = 3.48$, respectively. The permittivity of silver is described by the Drude model $\epsilon_2 = \epsilon_\infty - \omega_p^2 / (\omega(\omega + i\gamma))$ with permittivity $\epsilon_\infty = 3.7$, the plasmon frequency $\omega_p = 1.38 \times 10^{16}$ rad/s, and the damping factor $\gamma = 2.73 \times 10^{13}$ rad/s [31,32]. For simplicity, the loss of silver is ignored in the following calculations. However, we

note that the loss does not affect the results qualitatively but quantitatively.

Figure 1(b) shows the transverse magnetic (TM) band structure of the proposed waveguide arrays. The results are obtained by the theoretical transfer matrix method (TMM) [33,34] and the Bloch theorem (see details in Appendix A). Here, we have set the geometrical parameters as $d_1 = 50$ nm, $d_2 = 10$ nm, $d_3 = 50$ nm, and $d_4 = 200$ nm, and the superlattice structure period as $\Lambda = 310$ nm. Note that the silicon layer with such a relatively large width d_4 can support high-order photonic modes in the considered wavelength region ($\lambda = 500$ – 1500 nm). The multiple bands in Fig. 1(b) result from the mutual interactions between the second-order, first-order, and zero-order photonic modes in the silicon slab and the symmetric (even) and antisymmetric (odd) surface plasmon polariton (SPP) modes in the sandwich dielectric-metal-dielectric part [35]. It is seen that the neighboring bands touch and cross at Bloch wavevector $k_x = 0$ (BZ center) or $k_x = \pi/\Lambda$ (BZ edge).

To examine the band structure more specifically, firstly, we focus on the case of wavelength $\lambda = 500$ nm. The equiprobability contours (EFCs) are shown in Fig. 2(a), which is simply a z slice of Fig. 1(b). For simplicity, only positive propagation constants k_y are presented. It is seen that four branches of the EFC for the waveguide arrays are presented. In Fig. 2(a), we have labeled them consequently from 1 to 4, by the sequence of decreasing k_y . The H_z field distributions of the eigenstates at the BZ center for each band are plotted in the insets of Fig. 2(a), where the geometrical center of the unit cell is selected as the center of the silver layer [see Fig. 1(a)]. From these eigenstate patterns, it is quite easy to identify the coupling mechanisms. More specifically, the first band (band 1) and the second band (band 2) originate from the interaction between the zero-order photonic mode and the odd and even SPP mode, respectively. While the third band (band 3) is ascribed to the interaction between the first-order photonic mode and the odd SPP mode, and the fourth band (band 4) is ascribed to the interaction between the second-order photonic mode and the even SPP mode [35]. Overall, regarding the eigenstate symmetry with respect to the x direction, the modes belonging to bands 1 and 3 are of odd symmetry; and on the contrary, the modes belonging to bands 2 and 4 are of even symmetry.

To analyze the diffraction and deflection of a light beam coming from free space (air), it is instructive to superimpose the light dispersion in Fig. 2(a), wherein we have shown an additional green semicircle which represents the EFC in air. It should be emphasized that bands 1 and 2 in Fig. 2(a) are approximately flat. For these flat bands, the propagation of an incident beam with an arbitrary incident angle mostly keeps propagating along the y axis in the structure. This is determined by the conservation of the Bloch wave number k_x along the interface and the direction of group velocity [see the small arrows in Fig. 2(a)]. Figure 2(b) shows the full wave calculated results using the finite element method (FEM) for light propagation with a normal incident ($\theta = 0^\circ$) Gaussian beam. It keeps approximately straight and diffractionless after injecting into the structure since both bands 3 and 4 have group velocity toward the $+y$ direction near $k_x = 0$. Slight diffraction is visible which originates from bands 3 and 4.

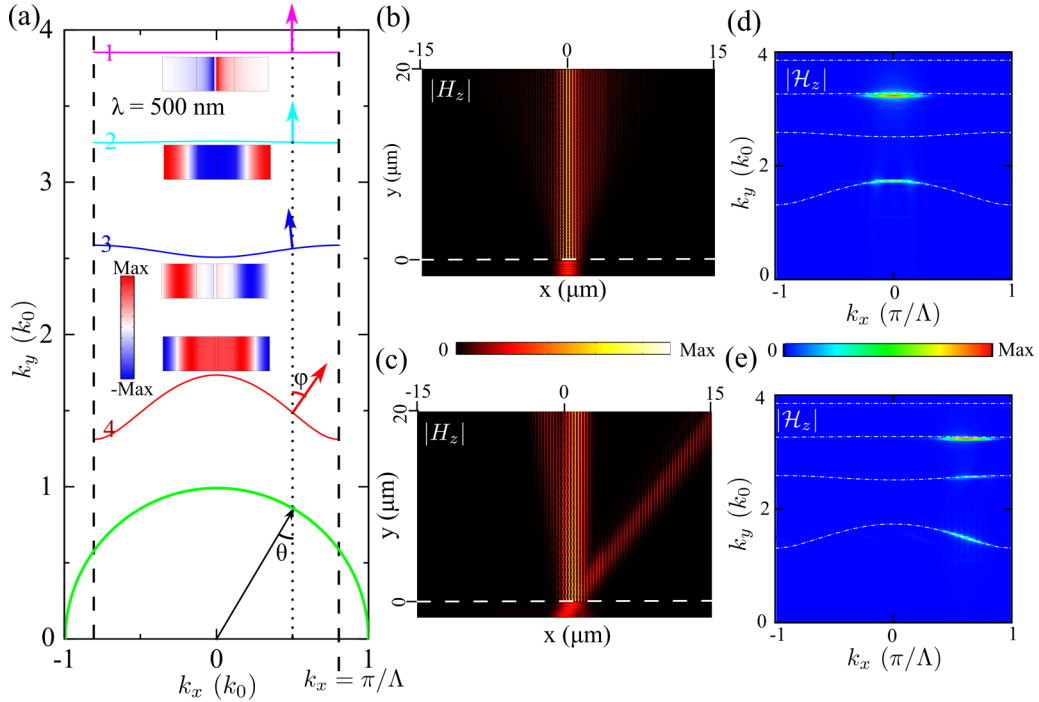


FIG. 2. Beam propagation analysis and dynamics simulation for $\lambda = 500$ nm. (a) Equifrequency contours (EFCs) in the waveguide arrays and free space. Insets are $|H_z|$ patterns of the corresponding eigenmode at $k_x = 0$. (b) and (c) Gaussian beam excitation and diffraction pattern in the structure. The horizontal dashed line marks the structure-air interface. (d) and (e) Spatial Fourier spectra \mathcal{H}_z of the diffraction patterns in (c) and (d). (b) and (d) are for normal incidence, while (c) and (e) are for incident angle $\theta = 30^\circ$. Dash-dotted curves are the calculated EFC by the semi-analytical transfer matrix method (TMM) approach.

However, as the incident angle is set to $\theta = 30^\circ$, the incident beam branches right at the incident port to an angle $\varphi \approx 39^\circ$ [see Fig. 2(c)], in addition to the normal propagation. These deflections have been marked by the vertical dotted line in Fig. 2(a), which intersects with band 4 and predicts the diffraction direction guided by the red arrow.

To carefully analyze the compositions of the refracted beams, we have calculated the Fourier transform of the H_z distribution in Figs. 2(b) and 2(c). The corresponding spatial Fourier spectra $|\mathcal{H}_z|$ are shown in Figs. 2(d) and 2(e), respectively. Clearly, for normal incidence, only the modes belonging to bands 2 and 4 are excited. This is in accord with the expectation from the mode symmetry analysis: as revealed in Fig. 1(a), in reference to the unit cell center (e.g., silver layer center), both the mode patterns and the Gaussian beam field are of even symmetry in the x direction. Modes in bands 1 and 3 are of odd symmetry and not excitable due to symmetry mismatch. On the contrary, for oblique incidence, one would expect that modes in all bands (1–4) are involved in the excitation. However, it is seen in Fig. 2(e) that the Fourier component is not obvious (almost invisible) in band 1. We ascribe this to possible weak excitation due to the extremely high k_y (in this case $k_y \approx 4k_0$), although the beam scattering at the structure-air boundary could generate arbitrary high- k diffraction components into both directions.

To investigate the frequency-dependent characteristics, we further increase the wavelength. Particularly, at $\lambda = 607.83$ nm, which cuts through a DP at the BZ center, the bands 1 and 2 cross each other at this degeneracy point. Due to the linear intersection in the vicinity of the BZ center, a normal

incident Gaussian beam would produce the conicallike beam diffraction that mimics a massless Dirac particle [36,37], as shown in Fig. 3(a). Simultaneously, there remain some side diffractions along with the main branches. Again, the origin can be identified through the spatial Fourier spectrum shown

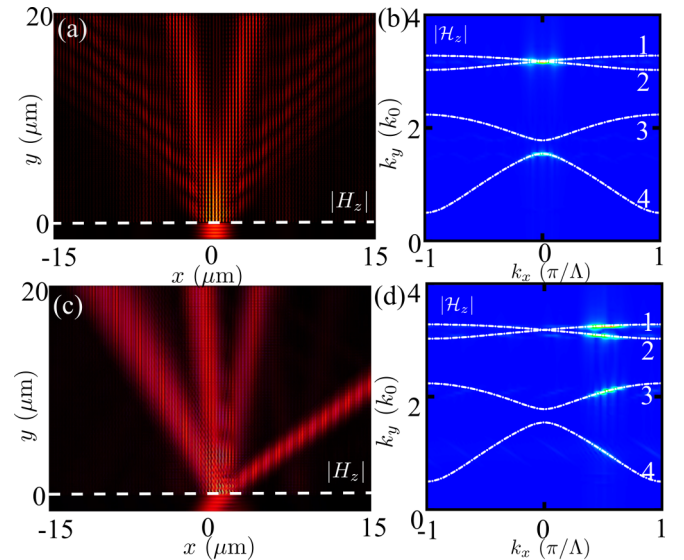


FIG. 3. Simulated beam dynamics for $\lambda = 607.83$ nm. (a) and (c) $|H_z|$ pattern and (b) and (d) the corresponding spatial Fourier spectra. The incident angle for the upper and lower panels are 0° and 30° , respectively.

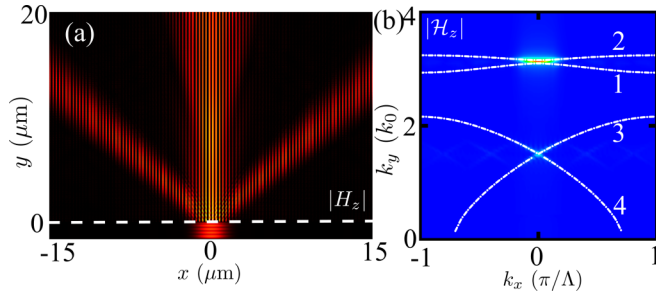


FIG. 4. Simulated beam dynamic for $\lambda = 634.9$ nm. (a) $|H_z|$ pattern and (b) the corresponding spatial Fourier spectra \mathcal{H}_z by the normal incidence of Gaussian beam.

in Fig. 3(b). The EFC of the structures at $\lambda = 607.83$ nm is also superimposed as dash-dotted (white) curves. Clearly, in addition to modes near the linear intersection point between bands 1 and 2, the modes belonging to band 4 are excited, which are allowed by symmetry, yet modes in band 3 remain unexcitable, as protected by symmetry.

Due to the distinct slopes of the dispersive bands, the diffracted wave of an oblique incident beam can be efficiently split into four branches. Figure 3(c) shows the beam propagation with the specific incident angle $\theta = 30^\circ$. Four main branches are observed: two are on the left side of the y axis, and the other two are on the right, representing negative and positive refractions, respectively. The components and the direction of these refractions can be obtained by the Fourier transform in Fig. 3(d), which is consistent with the EFC of the structure at $\lambda = 607.83$ nm. We have found that the multibranching behaviors are not sensitive to the silver loss but show different decaying rate for diffractive beams at the large angle and the small angle. The details are referred to in Appendix B.

Note that, as the wavelength increases, bands 3 and 4 continue to approach, and the gap is reduced, and they finally merge into another DP at $\lambda = 634.9$ nm. Certainly, conicallike beam diffraction is still observed upon the normal incidence of the Gaussian beam, as shown in Fig. 4(a). Additionally, we see a large portion of light propagating along the y axis. The

origin of the beam behaviors is clarified by the spatial Fourier spectrum shown in Fig. 4(b). From the superimposed EFC of the structures, we can conclude that the modes in bands 2, 3, and 4 are excited noticeably. However, in contrast to Fig. 2(a), the x direction symmetry of the modes belonging to the upmost band at the BZ center is changed to even. To distinguish these bands, we label these bands based on the symmetry of the eigenstates at BZ center. Then bands 1 and 2 are switched with respect to the results in Fig. 2. At the same time, band 1 is approximately flat around the BZ center, which gives rise to the central portion of the diffractive wave in Fig. 4(a). On the other hand, the crossing cone angle is larger than that in Fig. 3, which is responsible for the large refraction angle for the two obvious side branches in Fig. 4(a).

Particularly, we note that band 4 in Fig. 4(b) is gradually absent from the BZ edge. Indeed, it could be totally absent across the entire BZ as the wavelength keeps increasing. For instance, Fig. 5 shows the results for wavelength $\lambda = 700$ nm. Figure 5(a) shows the propagation pattern of a normal incident Gaussian beam. Figure 5(b) shows the EFC-superimposed Fourier transform of the propagation pattern in Fig. 5(a). It is seen that only modes in bands 2 and 4 are excited. Band 3 is totally not present in this working frequency.

III. PHOTONIC ZITTERBEWEGUNG EFFECT

From the propagation patterns and the associated spatial Fourier spectra, we have clearly demonstrated the various beam dynamics with respect to the frequency-dependent evolution of the EFC. Additionally, the coherent coupling between the excited eigenstates may lead to beam oscillation. It has been revealed that an optical analog of the Zitterbewegung effect resembles the trembling motion of Dirac electrons caused by the interference between the positive and negative energy states [2]. Note that the beam propagation in the multilayered systems shows oscillation patterns at the frequency either below or above the DP, due to the back-and-forth coherent coupling between the symmetric and antisymmetric modes [38]. To characterize the associated beam oscillation in our ternary plasmonic-dielectric waveguide arrays, the oscillation of the beam is described by the beam center defined

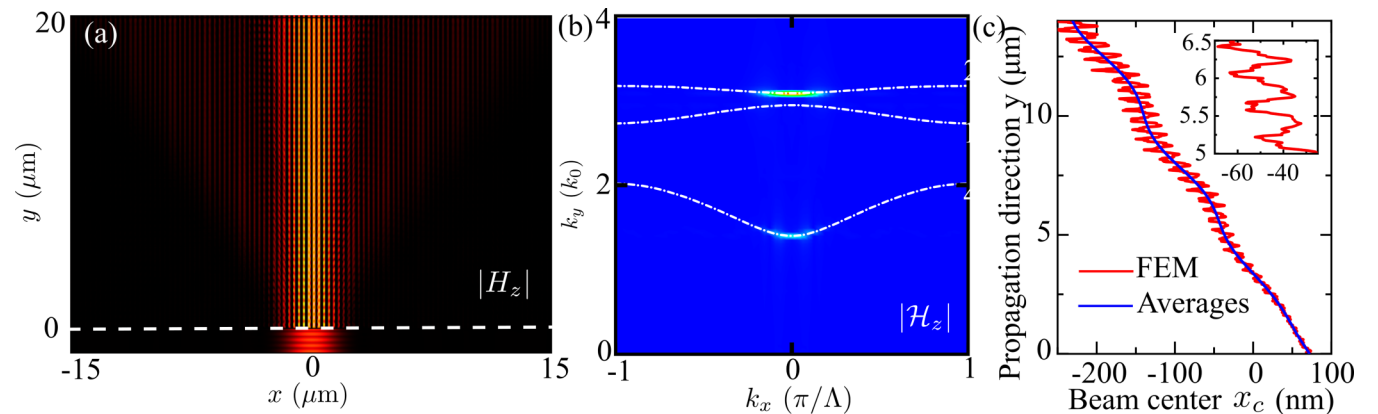
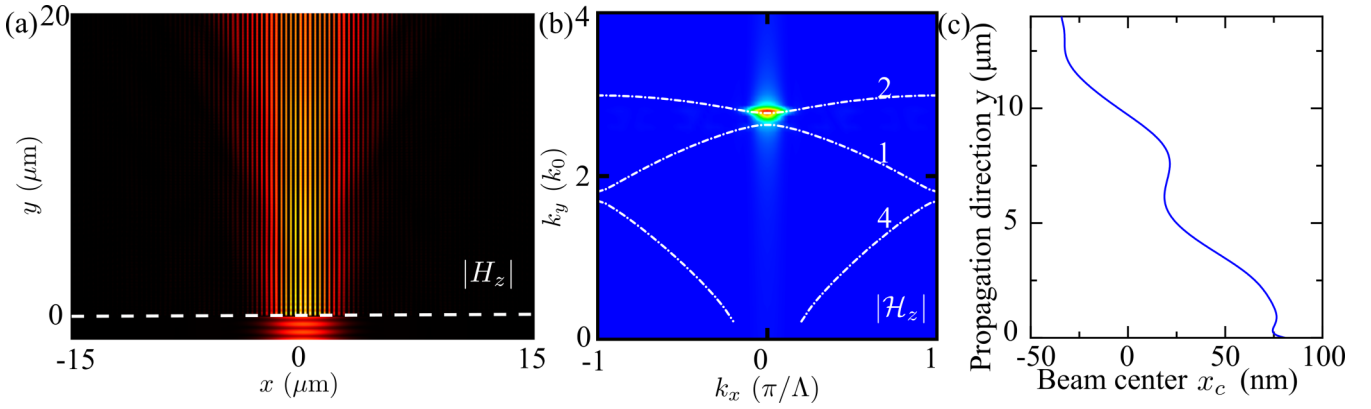


FIG. 5. Simulated beam dynamic for $\lambda = 700$ nm. (a) $|H_z|$ pattern and (b) the corresponding spatial Fourier spectra \mathcal{H}_z by the normal incidence of Gaussian beam. (c) The trajectory of the beam center x_c in the waveguide array. The red curves are the finite element method (FEM) results, and the blue is the corresponding averages of the positions.


 FIG. 6. Like Fig. 5 but with an alternative wavelength $\lambda = 1000$ nm.

as [38,39]

$$x_c(y) = \int_{-\infty}^{+\infty} |\mathbf{E}(x)|^2 x dx / \int_{-\infty}^{+\infty} |\mathbf{E}(x)|^2 dx. \quad (1)$$

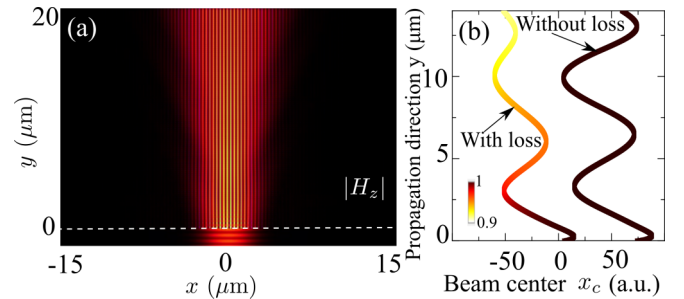
Generally, symmetric and antisymmetric modes at the BZ edge or center in the vicinity of DPs contribute to the beam propagation patterns of the Zitterbewegung effect, while for the case of normal incidence, the antisymmetric mode cannot be excited as discussed in the proceeding part. To excite the antisymmetric mode at the BZ center, breaking the symmetry protection between the source and the antisymmetric mode is necessary. Laterally shifting the center of the Gaussian beam away from the center of the unit cell and adding a slight angle of the incident beam are two feasible schemes. Here, we choose an incident angle $\theta = 0.5^\circ$ for the demonstration. Figure 5(c) plots the obtained beam center $x_c(y)$ vs the propagating distance y , as extracted from the wave dynamics simulation with the FEM [e.g., like Fig. 5(a)]. Clearly, the trajectory (red curve) vibrates differently from those in previously reported work [2,38]. To elucidate the origin, we further analyze the components of the involved modes. Due to the oblique incidence, the modes of bands 2 and 1 around $k_x = 0$ are excited with $k_{y2} \approx 3.083k_0$ and $k_{y1} \approx 2.941k_0$ in Fig. 5(b). The back-and-forth coherent coupling between these two modes can lead to the oscillation of the propagating pattern with an approximate period $\eta = 2\pi/\Delta k_y = 2\pi/(k_{y2} - k_{y1}) \approx 4933$ nm. This coincides with the period of the blue curve (the averages of the beam center positions) in Fig. 5(c). Simultaneously, the mode with $k_{y4} \approx 1.4k_0$ belonging to band 4 is excited $k_{y3} = 1.4k_0$ and coherently coupled with the mode in band 2. The corresponding period of beam center measured by $x_c(y)$ is $\eta = 2\pi/(k_{y2} - k_{y4}) \approx 416$ nm. This also coincides with the FEM simulation results, as shown in the inset of Fig. 5(c). The coherent coupling among modes in the three different bands can produce faster vibration of the beam center. This serves as the extension of the photonic Zitterbewegung effect to cases of more than two bands.

The three-mode coupling case is reduced to the two-mode coupling case with further increased wavelength. Here, we select $\lambda = 1000$ nm as an example. Figure 6(a) shows the propagation pattern like that in Fig. 5(a). In this case, the band dispersion is superimposed in Fig. 6(b). Clearly, band 4 is

absent around the BZ center, and only two modes belonging to bands 1 and 2 contribute to the oscillation of the beam center, as shown in Fig. 6(c). Like Fig. 5, to excite the antisymmetric mode of band 1, a small angle is introduced into the Gaussian beam. In such a case, the eigenmodes at the BZ center with the propagation constants $k_{y2} \approx 2.767k_0$ and $k_{y1} \approx 2.625k_0$ are excited, and the induced Zitterbewegung effect has oscillation period $\eta = 2\pi/(k_{y2} - k_{y1}) \approx 7042$ nm. This is also consistent with the FEM result shown in Fig. 6(c).

Another scheme to excite the antisymmetric mode is shifting the center of the incident beam away from the unit cell center laterally. In this case, we further analyze the effect of the damping factor in the Drude model on the beam propagation and the Zitterbewegung effect. Figure 7(a) shows the beam propagation pattern for the case of $\gamma = 2.73 \times 10^{13}$ rad/s used in the Drude model. The attenuation is not significant. Figure 7(b) clearly shows that the strength of the beam oscillation is significantly suppressed for the left colored curve, in contrast to the right curve for the exact case without loss. Certainly, the absorption loss of silver would affect the oscillation strength of the Zitterbewegung effect. However, the decaying is quite slow, in similarity to the case of hybrid SPP [40,41].

It is well known that the Zitterbewegung effect is expected to be observed around DP. In our case, the DP at BZ center locates at $\lambda = 607.83$ nm for bands 1 and 2. However, we


 FIG. 7. Simulated beam dynamic for $\lambda = 1000$ nm. (a) $|H_z|$ pattern and (b) the trajectory of the beam center x_c in the waveguide arrays. Here, the loss of silver is considered, namely, we use $\gamma = 2.73 \times 10^{13}$ rad/s. Color of the beam center curve indicates total power across the corresponding y plane.

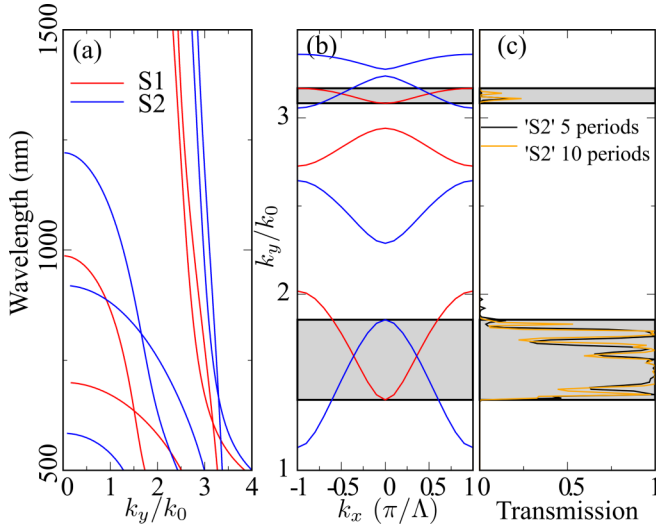


FIG. 8. (a) The band structure for the original waveguide array S1 (red curves) and the modified waveguide array S2 (blue curves). (b) The equipfrequency contours (EFCs) at the wavelength $\lambda = 700$ nm. (c) The transmission of the heterojunction S1-S2-S1 vs the propagation constant k_y . The gray regions in (b) and (c) indicate the overlapped EFCs of S1 and S2. The black (orange) curve in (c) is for the waveguide array S2 with periods 5 (10).

have demonstrated that the Zitterbewegung effect can happen not only related to the coherent coupling between two modes but may also be extended to the coherent coupling among three modes. Particularly, the oscillation of the beam center becomes more interesting than the prediction from the DP crossing from a two-band model. Indeed, the Zitterbewegung effect can be observed at the wavelength far away from the DP, for instance, $\lambda = 1250$ nm, which is shown in Appendix C. This is due to the mutual interactions among multiple modes and the resultant small bandgap around the degeneracy point exactly at $\lambda = 607.83$ nm. Additionally, the effects of the beam width, the offset between the centers of the unit cell and the Gaussian beam, and the loss of silver are carefully investigated and justify this observation (results can be found in Appendix D). Once the antisymmetric modes are excited, the Zitterbewegung effect can be observed easily in our system. The beam waist mainly influences the oscillation phase and has a negligible effect on the oscillation period. As for the different offsets, the oscillation patterns show fixed beam center profile. In addition to the losses of silver, the effects of the disorder in the thickness have also been carefully discussed in Appendix E.

IV. PHOTONIC KLEIN TUNNELING

The photonic analog of Klein tunneling has been unambiguously observed near DPs in waveguide arrays [26,29]. The unity transmission of the tunneling is usually observed in the heterojunction composed of sandwiched artificial structures with shifted DPs [42]. We note that, in the band structure of Fig. 1(b), the Dirac cones appear at the BZ center. As aforementioned, the lowest- λ DP is derived from the higher-order photonic modes in silicon waveguide. As such, the spectral position of this DP can be tuned by varying the

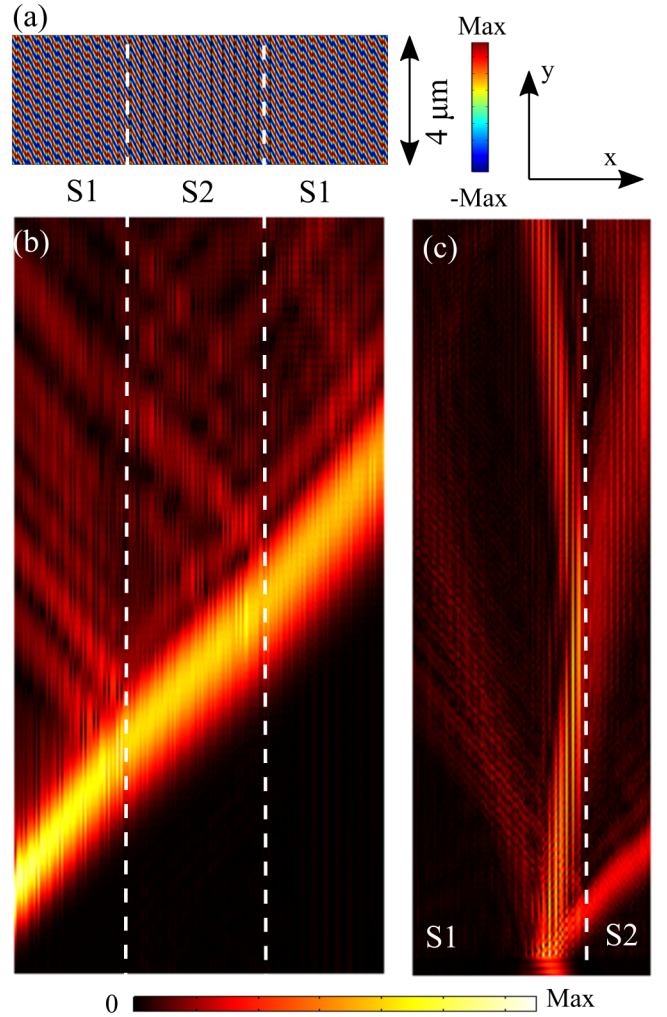


FIG. 9. (a) The field distribution of magnetic component H_z with $k_y = 1.54k_0$ in the heterojunction S1-S2-S1. (b) The intensity distribution of the field excited by the Gaussian source with a main propagation constant $k_y = 1.54k_0$. (c) The wave propagation with a Gaussian source incident into the interface between the air and the S1-S2 connection with an incident angle. The white dashed line indicates the interface between different waveguide arrays S1 and S2.

width of the silicon layer d_4 . We then choose modified waveguide arrays with $d_1 = d_3 = 35$ nm, $d_2 = 10$ nm, $d_4 = 280$ nm, termed S2, and the original waveguide arrays studied in Fig. 1(b) (termed S1) to construct a heterojunction. Figure 8(a) shows the results at the BZ center ($k_x = 0$) for the waveguide arrays S1 (red curves) and S2 (blue curves), respectively. The degeneracy between the symmetric and antisymmetric modes leads to band crossing, marking the emergence of DPs. The frequency for the presence of Klein tunneling falls between the dispersion curve intersections of two waveguide arrays [26]. Note that, for the upper bands, only one intersection is present, and this may contribute to the low transmission in the combined heterojunction discussed below.

Figure 8(b) shows the EFCs for wavelength $\lambda = 700$ nm that is between the two DPs in Fig. 8(a). When passing a potential barrier, the energy and momentum along the

interface are conserved. As such, the component of the waves k_y is fixed when the light passes through the interface between two different waveguide arrays. Therefore, one of the prerequisite conditions for the Klein tunneling is the overlapped EFCs between S1 and S2, i.e., the gray region in Fig. 8(b), sharing the same propagation constant k_y . To further characterize the tunneling efficiency, we calculate the transmission of the combined heterojunction S1-S2-S1 with different barrier width of S2. Note that the boundary condition is periodic along the y axis. Figure 8(c) shows the obtained transmission by TMM. Results of different width (5 and 10 periods) of the potential barrier, i.e., waveguide array S2, are both shown. Clearly, unity transmission for the lower gray zone can be achieved for both cases.

Figure 9(a) shows the H_z field profile with the propagation wavenumber $k_y = 1.54k_0$, locating at the lower zone in Fig. 8(c). Clearly, the wave can totally tunnel into the potential barrier (waveguide array S2 with 10 periods) and further tunnel into the waveguide array S1. To demonstrate the Klein tunneling more clearly, a Gaussian beam is launched into the heterojunction from the left port with an approximate propagation constant k_y along the interface. Figure 9(b) shows that a main portion of the power passes through the interface between S1 and S2 and subsequently between S2 and S1. Only a small portion of power is reflected, which mainly comes from the wide distribution of the wave vectors resulting from the finite-width Gaussian beam. Figure 9(c) shows the situation that the Gaussian beam obliquely incidents from the bottom of the waveguide arrays into waveguide array S1 (like the case in Fig. 2). Due to the multiple EFC branches, two dominant beams propagate toward the S1/S2 interface with different angles and refract since both fall in the tunneling zone (shaded region) shown in Fig. 8(b). The difference is that the large diffraction angle beam (the lower one) can nearly totally pass through the interface S1/S2, while only a portion of the small diffraction angle beam (the upper one) can tunnel into the waveguide array S2.

V. CONCLUSIONS

A few comments are in order before the conclusion. The efforts in this paper mainly focus on the beam dynamics modulated by the multiple mode interactions. Certainly, the ternary system and the abundant mode coupling dynamics can be extended to quasi-3D planar configuration and on-chip integrated systems. It is highly desirable to break the periodic symmetry to turn the structure toward the nonperiodic type. For example, one can expect optical Bloch oscillation by imposing linear gradient of the propagation constants via geometrical variation [43–45]. Furthermore, by involving modulation in additional dimensions such as the gain-loss degree of freedom, it is possible to explore parity-time symmetry-induced complicated non-Hermitian optical dynamics [46–48]. The interplay between the non-Hermiticity and topology degrees of freedom enables intriguing light propagation, including robust optical coupling and the topological modes [8,49–51]. Additionally, the imaginary-mass particles may be simulated in our system by extension to non-Hermitian waveguide arrays [52].

In summary, we have investigated the beam dynamics in ternary plasmonic-dielectric waveguide arrays. Due to the presence of the high-order photonic modes, interactions between the plasmonic and photonic modes give rise to the intriguing evolution of the band dispersion. Near the degeneracy around the BZ center and edge, a variety of beam propagation engineering can be achieved, including the angle-dependent beam branching/multibranching, conicallike beam diffraction. Furthermore, it is demonstrated that the Zitterbewegung effect induced by the coherent coupling between two modes around the DP is present for a wide wavelength range because of two very flat touching bands. Particularly, a fast vibration of the beam center acts as an extension of the typical Zitterbewegung effect due to the coherent coupling among extra modes that differs more in the propagation moment. Additionally, the appropriate unity transmission of the Klein tunneling can be observed. The strong frequency-dependent beam dynamics can be utilized to control on-chip light propagation control, including wave routing, selectively directional coupling, and multiplexing/demultiplexing.

ACKNOWLEDGMENTS

This paper was supported by the Shenzhen Municipal Science and Technology Plan (No. JCYJ20180306172003963), Natural Science Foundation of China (11274083), and Guangdong Natural Science Foundation (No. 2018A030313939).

APPENDIX A: DERIVATION OF THE DISPERSION RELATION

The TMM is utilized to obtain the band structure of the multilayered stacks, as shown in Fig. 1 of the main text. The relation between the incident and scattering waves can be characterized by a 2×2 matrix. Thus, the transfer matrix at the interface from layer m to layer n is given by

$$\mathbf{M}_{mn} = \frac{1}{2} \begin{bmatrix} \frac{1+v_{mn}}{v_{mn}} & \frac{-1+v_{mn}}{v_{mn}} \\ \frac{-1+v_{mn}}{v_{mn}} & \frac{1+v_{mn}}{v_{mn}} \end{bmatrix}, \tag{A1}$$

where $v_{mn} = \varepsilon_m k_n / \varepsilon_n k_m$, $k_m = \sqrt{k_0^2 \varepsilon_m - k_y^2}$, with $m = 1, 2, 3, 4$.

The propagation matrix in layer m is described by

$$\mathbf{M}_m = \begin{bmatrix} \exp(jk_m d_m) & 0 \\ 0 & \exp(-jk_m d_m) \end{bmatrix}, \tag{A2}$$

where d_m is the thickness of the layer m . Then the transfer matrix of a unit cell is

$$\mathbf{M} = \mathbf{M}_{41} \mathbf{M}_4 \mathbf{M}_{34} \mathbf{M}_3 \mathbf{M}_{23} \mathbf{M}_2 \mathbf{M}_{12} \mathbf{M}_1. \tag{A3}$$

According to the Bloch theorem, the dispersion relation can be expressed as

$$\cos(k_x \Lambda) = \frac{1}{2} \text{Tr}(\mathbf{M}), \tag{A4}$$

with k_x the Bloch wave vector, Λ the thickness of the lattice supercell, and $\text{Tr}(\mathbf{M})$ the trace of \mathbf{M} in Eq. (A3). To get the definite expression, we transfer Eq. (A3) into two parts; each

of them consists of two layers:

$$\mathbf{M}'_{12} = \mathbf{M}_{23}\mathbf{M}_2\mathbf{M}_{12}\mathbf{M}_1 = \begin{bmatrix} m_{11} & m_{12} \\ m_{21} & m_{22} \end{bmatrix}, \quad (\text{A5})$$

$$\mathbf{M}'_{34} = \mathbf{M}_{41}\mathbf{M}_4\mathbf{M}_{34}\mathbf{M}_3 = \begin{bmatrix} m'_{11} & m'_{12} \\ m'_{21} & m'_{22} \end{bmatrix}. \quad (\text{A6})$$

Each element of these two matrices reads

$$m_{11} = \frac{e^{j\kappa_1}}{2}[(v_{31} + 1) \cos \kappa_2 + j(v_{32} + v_{21}) \sin \kappa_2], \quad (\text{A7})$$

$$m_{12} = \frac{e^{-j\kappa_1}}{2}[(-v_{31} + 1) \cos \kappa_2 + j(v_{32} - v_{21}) \sin \kappa_2], \quad (\text{A8})$$

$$m_{21} = \frac{e^{j\kappa_1}}{2}[(-v_{31} + 1) \cos \kappa_2 + j(-v_{32} + v_{21}) \sin \kappa_2], \quad (\text{A9})$$

$$m_{22} = \frac{e^{-j\kappa_1}}{2}[(v_{31} + 1) \cos \kappa_2 - j(v_{32} + v_{21}) \sin \kappa_2], \quad (\text{A10})$$

$$m'_{11} = \frac{e^{j\kappa_3}}{2}[(v_{13} + 1) \cos \kappa_4 + j(v_{43} + v_{14}) \sin \kappa_4], \quad (\text{A11})$$

$$m'_{12} = \frac{e^{-j\kappa_3}}{2}[(-v_{13} + 1) \cos \kappa_4 + j(-v_{43} + v_{14}) \sin \kappa_4], \quad (\text{A12})$$

$$m'_{21} = \frac{e^{j\kappa_3}}{2}[(-v_{13} + 1) \cos \kappa_4 + j(v_{43} - v_{14}) \sin \kappa_4], \quad (\text{A13})$$

$$m'_{22} = \frac{e^{-j\kappa_3}}{2}[(v_{13} + 1) \cos \kappa_4 - j(v_{43} + v_{14}) \sin \kappa_4], \quad (\text{A14})$$

where $v_{mn} = \varepsilon_m k_n / \varepsilon_n k_m$ and $\kappa_m = k_m d_m$. From Eqs. (A7)–(A14), we can further simplify the expression if the first and the third layers are identical, i.e., $v_{13} = 1$. In this case, Eq. (A4) reads

$$\begin{aligned} \frac{4 \cos(k_x \Lambda)}{\Xi} = & 4 + \left(v_{24} + \frac{1}{v_{24}} - v_{21} v_{34} - \frac{1}{v_{21} v_{34}} \right) \frac{\tan \kappa_2 \tan \kappa_4 \cos(\kappa_1 - \kappa_3)}{\cos(\kappa_1 + \kappa_3)} - 2(v_{14} + v_{43}) \tan \kappa_4 \tan(\kappa_1 + \kappa_3) \\ & - 2(v_{21} + v_{32}) \tan \kappa_2 \tan(\kappa_1 + \kappa_3) - \left(v_{24} + \frac{1}{v_{24}} + v_{21} v_{34} + \frac{1}{v_{21} v_{34}} \right) \tan \kappa_2 \tan \kappa_4. \end{aligned} \quad (\text{A15})$$

APPENDIX B: LOSS EFFECT ON THE BEAM BRANCHING

In the main text, we have systematically investigated the multibranching of the beam propagation without considering the loss factor of silver. Considering the realistic case, the loss can affect the propagation. Here, we select the situation in Fig. 3(c) in the main text as an example to describe the effect of the reflection in the presence of loss in the silver layers. Figure 10 shows the corresponding beam propagation upon the oblique incident of the Gaussian beam. Clearly,

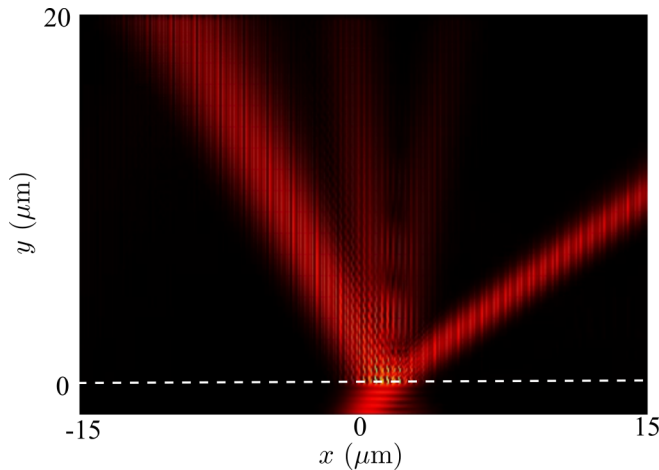


FIG. 10. Simulated $|H_z|$ pattern for $\lambda = 607.83$ nm in the presence of loss in the silver layer for incoming beam at incident angle 30° . The four-branched diffractive beam experiences distinct attenuation, depending on the corresponding mode pattern and its origin.

the multibranching behavior of the beam remains but with different damping rates for different branches. The central two branches originating from the upper two bands decay quite faster than the outer branches, resulting from the lower two bands. This is due to the different imaginary part of the eigenstates excited by the oblique incident beam. The free space k_0 normalized propagation constants are, respectively, $k_y/k_0 = 3.50 - 0.0237i$, $3.15 - 0.0016i$, $2.1 - 0.0009i$, and $1.03 - 0.0012i$ for the excited modes in bands 1, 2, 3, and 4. Clearly, those in bands 3 and 4 have relatively small imaginary parts. In other words, the refracted beams originating from the lower two bands can propagate with less attenuation (see Fig. 10).

APPENDIX C: PHOTONIC ZITTERBEWEGUNG EFFECT IN A WIDE WAVELENGTH RANGE

It is quite interesting that the system we proposed supports the Zitterbewegung effect for operating wavelength from around $\lambda = 700$ to 1500 nm, enabled by the fact that the two bands 1 and 2 in Fig. 1(b) are flat and nearly parallel. This could be an ideal platform for experimental observation since it is not sensitive to the working frequency. Figure 11 shows the case for $\lambda = 1250$ nm.

APPENDIX D: EFFECTS OF BEAM CENTER OFFSET AND BEAM WIDTH ON THE ZITTERBEWEGUNG EFFECT

As described in the main text, we have mentioned that there are two different schemes for breaking the phase mismatching between the Gaussian beam and the antisymmetric mode. The details for the scheme by introducing a nonzero incident angle

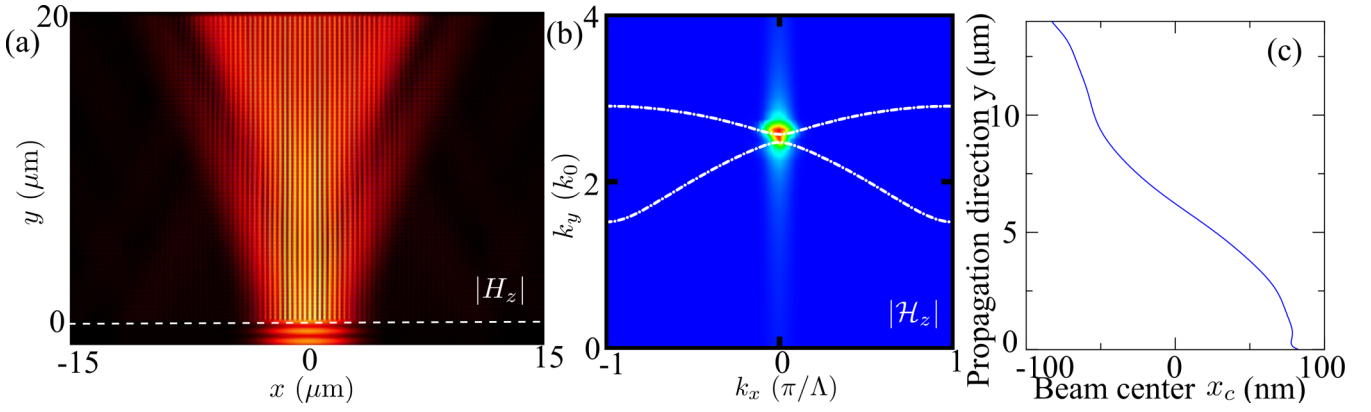


FIG. 11. Simulated beam dynamic for $\lambda = 1250$ nm. (a) $|H_z|$ pattern and (b) the corresponding spatial Fourier spectra \mathcal{H}_z by the normal incidence of Gaussian beam. (c) The trajectory of the beam center x_c in the waveguide array.

are described in the main text. Here, we focus on the other scheme. Moving the center of the incident beam away from the unit cell center can also lead to the excitation of the anti-symmetric mode. Figure 12(a) shows the beam dynamics for a specific offset distance $\Delta x = -50$ nm between the centers of the unit cell and the normal incident beam center. Clearly, the propagation pattern is like Fig. 6(a). From the trajectory of the beam center in Fig. 11(b), we can find that the beam center exhibits similar oscillation for $\Delta x = -50, -100$, and -150 nm. All cases have the same oscillation period as that in Fig. 6(c).

To investigate the effects of the offset distance Δx and the incident Gaussian beam width w_0 on the photonic Zitterbewegung effect, we have chosen three different offsets to examine the propagation and oscillation. Figure 12(b) clearly shows the offset Δx does not affect the oscillation pattern for the fixed incoming beam profile.

Notice that the Gaussian beam can be regarded as a superposition of plane wave directed toward different angles deviating from the beam axis. For a narrow beam waist, it contains more of a high transverse moment component, while for a wider beam waist, it approximately represents a plane wave going along the beam axis. Therefore, the beam waist would affect the diffraction and beam dynamics in the struc-

ture. Provided that the antisymmetric mode is excited and is coherently coupled with the symmetric mode, the Zitterbewegung effect is always observed. Figure 12(c) shows that different beam width mainly influences the oscillation phase and has a negligible effect on the oscillation period.

APPENDIX E: EFFECTS OF DISORDER

In addition to the losses, the relatively small technological fabrication imperfections do not dramatically change the bulk band structure and may give rise to additional defect states. To demonstrate these, we further investigate the structure by introducing some disorder. In the structure under the incident beam coverage, a thickness shift $\delta d = 0.05d_1$ is introduced for the silica layer, i.e., the thicknesses of the silica layers shown in the inset of Fig. 13 are set to, respectively, $d_2 + \delta d$ and $d_1 - \delta d$. Figure 13(a) shows the full wave simulated beam branching dynamics. Clearly, the main refracted beams are consistent with the periodic case [like Fig. 3(c)]. Simultaneously, there exists an additional branch which propagates along the y direction. This is due to the defect states induced by the disorder of the lattice. In terms of the photonic Zitterbewegung effect, the disorder plays a significant role in the excitation of the Zitterbewegung effect. In Appendix D,

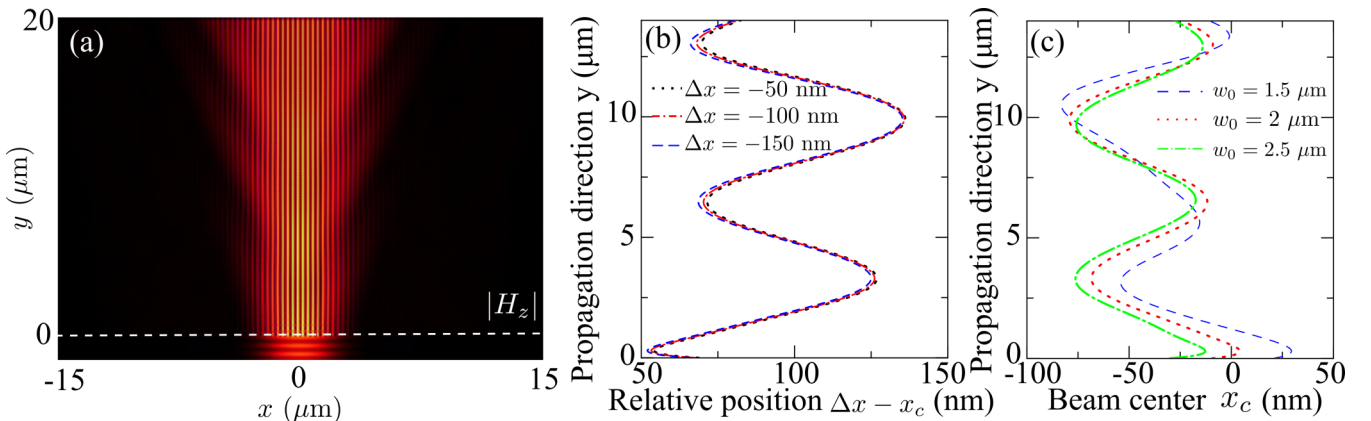


FIG. 12. Full wave simulated beam dynamic for $\lambda = 1000$ nm. (a) $|H_z|$ pattern and (b) the trajectory of the beam center x_c in the waveguide array.

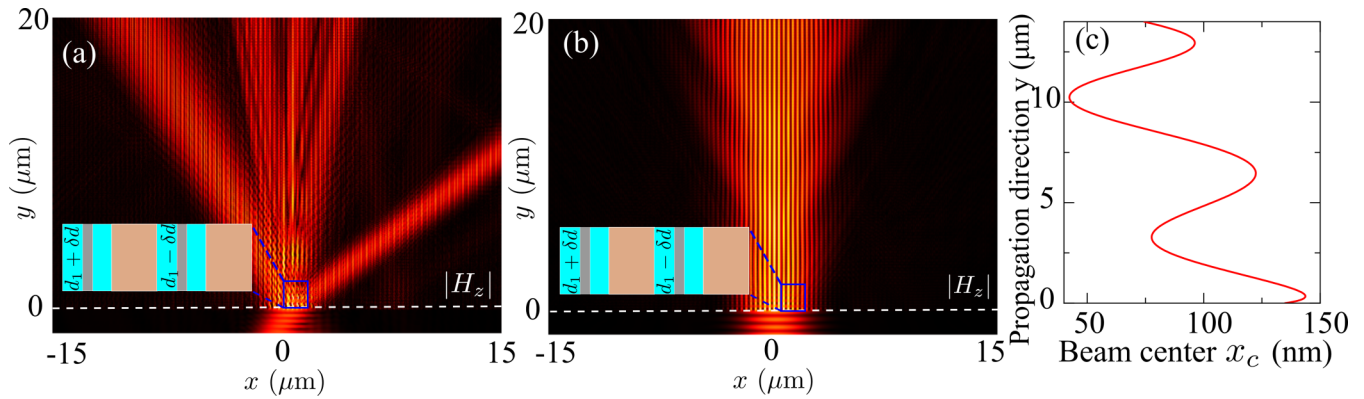


FIG. 13. Simulated beam dynamics of the disorder in the thickness. (a) $|H_z|$ pattern at $\lambda = 607.83$ nm and incident angle $\theta = 30^\circ$. (b) $|H_z|$ pattern at $\lambda = 1000$ nm and (c) the obtained beam center x_c in the waveguide array. Inset shows the applied disorder in the thickness of the silica layer.

it has been illustrated that the offset between the incident beam center and unit cell center can lead to the excitation of the antisymmetric mode and the resultant beam oscillation. Here, the introduction of structure disorder breaks the sym-

metry confinement; therefore, the coherent coupling of the modes in the vicinity of the DPs is induced, and the resultant beam oscillation can be observed as shown in Figs. 13(b) and 13(c).

-
- [1] P. Hannan and M. Balfour, *IEEE T. Antenn. Propag.* **13**, 342 (1965).
- [2] S. Longhi, *Opt. Lett.* **35**, 235 (2010).
- [3] I. L. Garanovich, S. Longhi, A. A. Sukhorukov, and Y. S. Kivshar, *Phys. Rep.* **518**, 1 (2012).
- [4] D. N. Christodoulides, F. Lederer, and Y. Silberberg, *Nature* **424**, 817 (2003).
- [5] R. Iwanow, D. A. May-Arrijo, D. N. Christodoulides, G. I. Stegeman, Y. Min, and W. Sohler, *Phys. Rev. Lett.* **95**, 053902 (2005).
- [6] L. Sun, J. Gao, and X. Yang, *Opt. Express* **21**, 21542 (2013).
- [7] Q. Cheng, Y. Pan Pan, Q. Wang, T. Li, and S. Zhu, *Laser Photonics Rev.* **9**, 392 (2015).
- [8] W. Song, W. Sun, C. Chen, Q. Song, S. Xiao, S. Zhu, and T. Li, *Laser Photonics Rev.* **14**, 1900193 (2020).
- [9] M. Xiao, Z. Q. Zhang, and C. T. Chan, *Phys. Rev. X* **4**, 021017 (2014).
- [10] X. Fan, G. P. Wang, J. C. W. Lee, and C. T. Chan, *Phys. Rev. Lett.* **97**, 073901 (2006).
- [11] H. Shin and S. Fan, *Appl. Phys. Lett.* **89**, 151102 (2006).
- [12] W. Yang, X. Shi, H. Xing, and X. Chen, *Plasmonics* **14**, 441 (2019).
- [13] G. Bartal, G. Lerosey, and X. Zhang, *Phys. Rev. B* **79**, 201103(R) (2009).
- [14] L. Verslegers, P. B. Catrysse, Z. Yu, and S. Fan, *Phys. Rev. Lett.* **103**, 033902 (2009).
- [15] A. Block, C. Etrich, T. Limboeck, F. Bleckmann, E. Soergel, C. Rockstuhl, and S. Linden, *Nat. Commun.* **5**, 3843 (2014).
- [16] S. H. Nam, E. Ulin-Avila, G. Bartal, and X. Zhang, *Opt. Express* **18**, 25627 (2010).
- [17] H. Deng, X. Chen, N. C. Panoiu, and F. Ye, *Opt. Lett.* **41**, 4281 (2016).
- [18] S. H. Nam, J. Zhou, A. J. Taylor, and A. Efimov, *Opt. Express* **18**, 25329 (2010).
- [19] S. H. Nam, E. Ulin-Avila, G. Bartal, and X. Zhang, *Opt. Lett.* **35**, 1847 (2010).
- [20] Z. Zhang, M. H. Teimourpour, J. Arkininstall, M. Pan, P. Miao, H. Schomerus, R. El-Ganainy, and L. Feng, *Laser Photonics Rev.* **13**, 1800202 (2019).
- [21] G. Della Valle and S. Longhi, *Opt. Lett.* **35**, 673 (2010).
- [22] X. Shi, W. Yang, H. Xing, and X. Chen, *Opt. Lett.* **40**, 1635 (2015).
- [23] C. Li, R. Cui, F. Ye, Y. V. Kartashov, L. Torner, and X. Chen, *Opt. Lett.* **40**, 898 (2015).
- [24] W. Song, H. Li, S. Gao, C. Chen, S. Zhu, and T. Li, *Adv. Photon.* **2**, 036001(2020).
- [25] S. H. Nam, A. J. Taylor, and A. Efimov, *Opt. Express* **18**, 10120 (2010).
- [26] L. Sun, J. Gao, and X. Yang, *Sci. Rep.* **7**, 9678 (2017).
- [27] X. Zhang, *Phys. Rev. Lett.* **100**, 113903 (2008).
- [28] F. Dreisow, M. Heinrich, R. Keil, A. Tunnermann, S. Nolte, S. Longhi, and A. Szameit, *Phys. Rev. Lett.* **105**, 143902 (2010).
- [29] S. Longhi, *Phys. Rev. B* **81**, 075102 (2010).
- [30] N. Wang, R.-Y. Zhang, C. T. Chan, and G. P. Wang, *Phys. Rev. B* **102**, 094312 (2020).
- [31] P. B. Johnson and R. W. Christy, *Phys. Rev. B* **6**, 4370 (1972).
- [32] Z. Chen, R. Hu, L. Cui, L. Yu, L. Wang, and J. Xiao, *Opt. Commun.* **320**, 6 (2014).
- [33] Z. Liu, Q. Zhang, F. Qin, D. Zhang, X. Liu, and J. J. Xiao, *Phys. Rev. A* **99**, 043828 (2019).
- [34] Z. Liu, Q. Zhang, F. Qin, D. Zhang, X. Liu, and J. J. Xiao, *Phys. Rev. B* **99**, 085441 (2019).
- [35] Z. Liu, G. Wei, D. Zhang, and J. J. Xiao, *Opt. Express* **28**, 37474 (2020).
- [36] J. M. Zeuner, N. K. Efremidis, R. Keil, F. Dreisow, D. N. Christodoulides, A. Tunnermann, S. Nolte, and A. Szameit, *Phys. Rev. Lett.* **109**, 023602 (2012).
- [37] B. Xu, T. Li, and S. Zhu, *Opt. Express* **26**, 13416 (2018).

- [38] L. Sun, J. Gao, and X. Yang, *Opt. Express* **24**, 7055 (2016).
- [39] H. Deng, F. Ye, B. A. Malomed, X. Chen, and N. C. Panoiu, *Phys. Rev. B* **91**, 201402(R) (2015).
- [40] J. Du and J. Wang, *Opt. Express* **25**, 30124 (2017).
- [41] N. T. Huong, N. D. Vy, M.-T. Trinh, and C. M. Hoang, *Opt. Commun.* **462**, 125335 (2020).
- [42] X. Jiang, C. Shi, Z. Li, S. Wang, Y. Wang, S. Yang, S. G. Louie, and X. Zhang, *Science* **370**, 1447 (2020).
- [43] U. Peschel, T. Pertsch, and F. Lederer, *Opt. Lett.* **23**, 1701 (1998).
- [44] S. Longhi, M. Marangoni, M. Lobino, R. Ramponi, P. Laporta, E. Cianci, and V. Foglietti, *Phys. Rev. Lett.* **96**, 243901 (2006).
- [45] M. J. Zheng, J. J. Xiao, and K. W. Yu, *Phys. Rev. A* **81**, 033829 (2010).
- [46] Z. Liu, Q. Zhang, X. Liu, Y. Yao, and J. J. Xiao, *Sci. Rep.* **6**, 22711 (2016).
- [47] Z. Liu, Q. Zhang, Y. Chen, and J. J. Xiao, *Photonics Res.* **5**, 57 (2017).
- [48] Z. Fu, N. Fu, H. Zhang, Z. Wang, D. Zhao, and S. Ke, *Appl. Sci.* **10**, 3425 (2020).
- [49] W. Song, W. Sun, C. Chen, Q. Song, S. Xiao, S. Zhu, and T. Li, *Phys. Rev. Lett.* **123**, 165701 (2019).
- [50] N. Fu, Z. Fu, H. Zhang, Q. Liao, D. Zhao, and S. Ke, *Opt. Quant. Electron* **52**, 61 (2020).
- [51] S. Ke, D. Zhao, J. Liu, Q. Liu, Q. Liao, B. Wang, and P. Lu, *Opt. Express* **27**, 13858 (2019).
- [52] W. Song, S. Gao, H. Li, C. Chen, S. Wu, S. Zhu, and T. Li, *arXiv:2011.08496*.